Operational Multi-GNSS Global Ionosphere Maps at GFZ Derived from Uncombined Code and Phase Observations

Andreas Brack[1], Benjamin Männel[1], Jens Wickert[1,2], and Harald Schuh[1,2]

[1]GFZ German Research Centre for Geosciences, Potsdam, Germany
[2]Technische Universität Berlin, Institute of Geodesy and Geoinformation Science, Berlin, Germany

Key Points:

- Operational GFZ global VTEC maps from ground GNSS data are introduced
- A rigorous least-squares approach with uncombined multi-GNSS, multi-frequency code and phase data is applied
- A validation by means of a comparison with the IGS solution and Jason-3 altimetry VTEC data is provided

Corresponding author: Andreas Brack, `brack@gfz-potsdam.de`

Abstract

GNSS networks with multi-frequency data can be used to monitor the activity of the Earth's ionosphere and to generate global maps of the vertical total electron content (VTEC). This paper introduces and evaluates operational GFZ VTEC maps. The processing is based on a rigorous least-squares approach using uncombined code and phase observations, and does not entail leveling techniques. A single-layer model with a spherical harmonic VTEC representation is used. The solutions are generated in a daily post-processing mode with GPS, GLONASS, and Galileo data, and are provided for the period since the beginning of 2000. A comparison of the GFZ VTEC maps with the final combined IGS product shows a high consistency with the solutions of the IGS analysis centers. A validation with about four years of Jason-3 altimetry-derived VTEC data is provided, in which the GFZ solution has the smallest bias of 1.2 TEC units compared to the solutions of the IGS analysis centers, and with 3.0 TEC units one of the smallest standard deviations.

1 Introduction

Global navigation satellite systems (GNSS) are an effective tool to observe the Earth's ionosphere and measure its total electron content (TEC), e.g., Lanyi and Roth (1988); Sardon et al. (1994); Schaer et al. (1996); Davies and Hartmann (1997); Komjathy (1997); Mannucci et al. (1998); Hernández-Pajares et al. (1999); Jakowski et al. (1999). GNSS-derived TEC data provide valuable information for atmospheric studies or can be used to assess and mitigate the impact of the ionosphere on GNSS-based services such as positioning or tropospheric sounding.

Due to the presence of the instrumental code biases and the phase ambiguities, the unbiased line-of-sight or slant TEC (STEC) of the receiver-satellite links cannot be directly observed with GNSS, but only through applying an external model describing the spatiotemporal TEC distribution. It is common practice to use the geometry-free or L4 combination of the GPS L1 and L2 signals, which represent the STEC biased by respectively code biases and ambiguities for code and phase observations (Schaer, 1999). The ambiguities are usually removed from the model through leveling the phase to the code observations (Mannucci et al., 1998; Ciraolo et al., 2007). The so obtained leveled phase observations are then used to subsequently estimate the model coefficients and a set of estimable receiver and satellite code biases. The same technique can also be applied to dual-frequency data of other systems.

The disadvantages of this estimation strategy are that 1) it is limited to two frequencies, 2) it reduces the redundancy of the system, as one code and one phase observation are used in order to remove only one geometry parameter, and 3) it generally does not apply a weighting of the observations caused for instance by different elevation angles, see also the discussion in Khodabandeh and Teunissen (2016). Further, the temporal correlations introduced by the leveling operation seem to be generally ignored. A least-squares framework for multi-frequency TEC determination using a single receiver or a local array of receivers avoiding these shortcomings is presented in Khodabandeh and Teunissen (2016, 2017).

Global ionosphere maps (GIMs), containing a snapshot of the TEC in vertical direction (VTEC) on a spatial grid, are routinely generated by different institutes, for instance within the ionosphere working group of the International GNSS Service (IGS), see Hernández-Pajares et al. (2009) or Roma-Dollase et al. (2018) for an overview.

The German Research Centre for Geosciences (GFZ) Potsdam offers a wide range of products for ground and space based atmospheric sounding (Wickert et al., 2020). These efforts are now extended with operational ground-based GNSS GIMs, which are introduced and evaluated in this paper. The main focus and novelty of the paper is on the

formulation of a rigorous least-squares approach for the computation of multi-GNSS global VTEC maps based on the work in Khodabandeh and Teunissen (2016, 2017). The common single-layer ionospheric model with a spherical harmonic VTEC parameterization is employed. The GIMs are computed from GPS, GLONASS, and Galileo data for the period since 2000 and will be provided on an operational basis in the future. A high consistency with the GIMs of other analysis centers and the combined IGS solution is obtained. In a comparison with about four years of Jason-3 VTEC data, the GFZ solution has the smallest VTEC bias and one of the smallest standard deviations among the solutions by the IGS analysis centers.

In Section 2, the estimation framework and the ionospheric modeling approach are introduced. The processing settings and an analysis of the GFZ GIM product are presented in Section 3. A validation by means of a comparison with the IGS solution and Jason-3 VTEC data is given in Sections 4 and 5.

2 Methodology

In this section, the estimation framework for the GFZ GIMs is presented. We start with the GNSS observation equations and estimable parameters in Section 2.1 and the ionospheric modeling strategy in Section 2.2. The combination of these two parts yielding the unbiased TEC solutions is presented in Section 2.3.

2.1 GNSS Observation Equations and Estimable Parameters

The single-system GNSS code and phase observations $p_{r,j}^s$ and $\varphi_{r,j}^s$ between receiver r and satellite s on frequency f_j can be modeled as

$$
\begin{aligned}
\mathrm{E}\left[p_{r,j}^s(t)\right] &= \rho_r^s(t) + \mu_j i_r^s(t) + d_{r,j} + d_{\cdot,j}^s \\
\mathrm{E}\left[\varphi_{r,j}^s(t)\right] &= \rho_r^s(t) - \mu_j i_r^s(t) + a_{r,j}^s,
\end{aligned}
\tag{1}
$$

where t refers to the time of reception. A geometry-free representation is used, in which no information on the satellite-to-receiver geometry is employed. The link specific range parameters ρ_r^s contain all non-dispersive components such as the geometric ranges, the satellite and receiver clock offsets, and the tropospheric line-of-sight delays, which cannot be estimated separately. The first order ionospheric delays on the first frequency f_1 are denoted by i_r^s and are multiplied with $\mu_j = f_1^2/f_j^2$. The receiver and satellite code biases are denoted as $d_{r,j}$ and $d_{\cdot,j}^s$, and the ambiguity parameter $a_{r,j}^s = \delta_{r,j} + \delta_{\cdot,j}^s + \lambda_j N_{r,j}^s$ consists of the receiver and satellite phase biases $\delta_{r,j}$ and $\delta_{\cdot,j}^s$ and the integer ambiguity $N_{r,j}^s$, with λ_j the wavelength of frequency f_j. The integer ambiguities $N_{r,j}^s$ are constant for each cycle-slip free arc, and the instrumental code and phase biases are commonly assumed time-invariant (Montenbruck & Hauschild, 2013; Hauschild, 2017). Therefore, the time dependency is omitted for $d_{r,j}$, $d_{\cdot,j}^s$, and $a_{r,j}^s$. Phase wind-up, phase center offset and variation, and other frequency specific effects that cannot be captured in ρ_r^s are corrected a-priori.

We consider a network of receivers that observe the satellites on the frequencies f_j, $j = 1, \ldots, F$, with the objective to retrieve information about the state of the ionosphere. The system of equations resulting from Equ. 1 is rank deficient, implying that only certain linear combinations of the parameters can be unbiasedly estimated. In particular, the ionospheric slant delays $i_r^s(t)$ cannot be separated from the code biases $d_{r,j}$ and $d_{\cdot,j}^s$ and ambiguities $a_{r,j}^s$ and can therefore not be determined in an absolute sense. We make use of the invertible ionosphere-free (IF) and geometry-free (GF) decomposition of the code biases on the first two frequencies (Khodabandeh & Teunissen, 2015), shown for the receiver biases:

$$
d_{r,j} = d_{r,\mathrm{IF}} + \mu_j d_{r,\mathrm{GF}}, \quad j \le 2
\tag{2}
$$

Table 1. Estimable parameter combinations for arc-specific code biases.

Parameter		Definition	Condition
Ranges	$\tilde{\rho}_r^s(t)$	$\rho_r^s(t) + d_{r,\mathrm{IF}}^s$	
Ionospheric delays	$\tilde{i}_r^s(t)$	$i_r^s(t) + d_{r,\mathrm{GF}}^s$	
Code biases	$\tilde{d}_{r,j}^s$	$d_{r,j}^s - d_{r,\mathrm{IF}}^s - \mu_j d_{r,\mathrm{GF}}^s$	$j > 2$
Phase ambiguities	$\tilde{a}_{r,j}^s$	$a_{r,j}^s - d_{r,\mathrm{IF}}^s + \mu_j d_{r,\mathrm{GF}}^s$	

Table 2. Estimable parameter combinations with a receiver-satellite code bias decomposition; $(\cdot)_{1r} = (\cdot)_r - (\cdot)_1$.

Parameter		Definition	Condition
Ranges	$\tilde{\rho}_r^s(t)$	$\rho_r^s(t) + d_{r,\mathrm{IF}} + d_{\mathrm{IF}}^s$	
Ionospheric delays	$\tilde{i}_r^s(t)$	$i_r^s(t) + d_{r,\mathrm{GF}} + d_{\mathrm{GF}}^s$	
Rec. code biases	$\tilde{d}_{r,j}$	$d_{1r,j} - d_{1r,\mathrm{IF}} - \mu_j d_{1r,\mathrm{GF}}$	$r \neq 1, j > 2$
Sat. code biases	$\tilde{d}_{\cdot,j}^s$	$d_{\cdot,j}^s - d_{\mathrm{IF}}^s - \mu_j d_{\mathrm{GF}}^s$	
		$\quad + d_{1,j} - d_{1,\mathrm{IF}} - \mu_j d_{1,\mathrm{GF}}$	$j > 2$
Phase ambiguities	$\tilde{a}_{r,j}^s$	$a_{r,j}^s - (d_{r,\mathrm{IF}} + d_{\mathrm{IF}}^s) + \mu_j(d_{r,\mathrm{GF}} + d_{\mathrm{GF}}^s)$	

with

$$d_{r,\mathrm{IF}} = \frac{1}{\mu_2 - \mu_1}\left(\mu_2 d_{r,1} - \mu_1 d_{r,2}\right)$$

$$d_{r,\mathrm{GF}} = \frac{1}{\mu_2 - \mu_1}\left(-d_{r,1} + d_{r,2}\right). \tag{3}$$

The GF biases $d_{r,\mathrm{GF}}$ and d_{GF}^s are usually referred to as *differential code biases* (DCBs, e.g. Schaer (1999)). The rank deficiencies can for instance be removed by lumping the IF and GF code biases with $\rho_r^s(t)$ and $i_r^s(t)$, respectively. The resulting estimable parameter combinations are given in Table 1 and Table 2. In Table 1, the code biases $d_{r,j}^s = d_{r,j} + d_{\cdot,j}^s$ are assumed constant for each continuous satellite-receiver arc, so that receiver and satellite biases cannot be separated. The estimable ionospheric delays $\tilde{i}_r^s(t)$ are biased by the GF code biases. In Table 2, the code biases are assumed constant for the entire processing session, so that now receiver and satellite specific biases $\tilde{d}_{r,j}$ and $\tilde{d}_{\cdot,j}^s$ are estimable, which increases the redundancy. The biases of the first receiver are chosen as reference to remove the rank deficiencies. For now, this decomposition only affects the definition of the estimable code biases $\tilde{d}_{r,j}$ and $\tilde{d}_{\cdot,j}^s$, but there are further implications when introducing an ionospheric model, so that receiver and satellite GF code biases become estimable, see Section 2.3.

Infinitely many other estimable combinations of the parameters can be formulated, leading to different ionospheric parameters $\tilde{i}_r^s(t)$ that can be estimated with different precision (Khodabandeh & Teunissen, 2016, 2017). S-system theory tells us that there is a one-to-one correspondence between the parameters of different estimable parameter sets, so that solutions from different choices can be transformed to one another (Baarda, 1973; Teunissen, 1985) and can be used equivalently.

The extension to multi-GNSS is straightforward, since almost all parameters in Table 1 and 2 are link specific. The only exception are the receiver and satellite code biases $\tilde{d}_{1r,j}$ and $\tilde{d}_{\cdot,j}^s$ in Table 2, which are set up per constellation, as the receiver biases are not identical across systems.

2.2 Global Ionospheric Modeling

In order to obtain estimates of the unbiased TEC, the ionospheric delays $i_r^s(t)$ have to be separated from the GF code biases $d_{r,\mathrm{GF}}^s$, which is only possible through an ionospheric model, such as discussed in Hernández-Pajares et al. (2011). We use the common single-layer model (Davies & Hartmann, 1997; Mannucci et al., 1998; Schaer, 1999; Azpilicueta et al., 2006; Brunini & Azpilicueta, 2009, 2010; Goss et al., 2019), in which the TEC is assumed to be contained within an infinitesimal thin shell at a constant height, which we assume at 450 km above the mean Earth radius. The slant ionospheric delays $i_r^s(t)$ are assumed to be related to the vertical ionospheric delays $v_r^s(t)$ in radial direction via

$$i_r^s(t) = M(E_r^s(t))\, v_r^s(t), \tag{4}$$

with the modified single-layer mapping-function $M(\cdot)$ (Schaer, 1999) depending on the elevation angle $E_r^s(t)$. The global spatiotemporal distribution of the vertical ionospheric delays $v_r^s(t)$ is modeled with spherical harmonic basis functions as (Schaer, 1999)

$$v_r^s(t) = \sum_{n=0}^{n_{\max}} \sum_{m=0}^{n} P_{nm}\left(\sin\left(\phi_r^s(t)\right)\right) \left[c_{nm,k(t)}\cos\left(m\lambda_r^s(t)\right) + s_{nm,k(t)}\sin\left(m\lambda_r^s(t)\right)\right], \tag{5}$$

where $P_{nm}(\cdot)$ is the normalized associated Legendre function of degree n and order m, with a maximum degree of $n_{\max} = 15$. The latitude and longitude of the ionospheric pierce point (IPP) are denoted as $\phi_r^s(t)$ and $\lambda_r^s(t)$ and are expressed in a solar-geomagnetic reference frame, in which the z-axis points towards the north geomagnetic pole, the x-axis is in the plane containing the z-axis and the Sun, and the y-axis is positive towards dusk and completes a right-handed system (Laundal & Richmond, 2017). Freezing the position of the Sun reduces the temporal variations of the ionospheric delays and facilitates the modeling. The model coefficients are given by $c_{nm,k(t)}$ and $s_{nm,k(t)}$, where $k(t) \in \{1, \ldots, K\}$ represents the time interval that contains t, i.e., the observation span is partitioned into K intervals with constant coefficients.

The ionospheric delay $v_r^s(t)$ in [m] is linked to the $\mathrm{VTEC}_r^s(t)$ in [electrons/m^2] as

$$v_r^s(t) = 40.3 \frac{\mathrm{VTEC}_r^s(t)}{f_1^2}. \tag{6}$$

TEC values are usually given in TEC units ($1\,\mathrm{TECU} = 10^{16}$ electrons/m^2). The equivalent expression holds for $i_r^s(t)$ and the STEC. When multiple systems are used to estimate the ionospheric model coefficients in Equ. 5, it is important that all parameters $v_r^s(t)$ refer to the same reference frequency or are expressed directly in TECU.

2.3 Unbiased TEC Estimation

Estimating the unbiased STEC or, equivalently, the unbiased ionospheric slant delays $i_r^s(t)$ becomes possible when including the ionospheric model from Section 2.2 into the observation model from Section 2.1. We first focus on the model using arc-specific code biases $d_{r,j}^s$ without the receiver-satellite decomposition.

The estimable biased ionospheric delay parameters $\tilde{i}_r^s(t)$ for each arc and time instance in Table 1 are replaced by the K common sets of ionospheric model coefficients $c_{nm,\kappa}$ and $s_{nm,\kappa}$ from Eq. 5 and the GF code biases $d_{r,\mathrm{GF}}^s$ for each arc. The so defined set of parameters can be estimated unbiasedly from the network's observations using least-squares.

Let $\boldsymbol{b}_r^s(t)$ be a vector containing the known values of the mapping function times the basis functions from Eq. 4 and 5, and let $\boldsymbol{c}_{k(t)}$ be a vector of the same size with the associated coefficients $c_{nm,k(t)}$ and $s_{nm,k(t)}$, so that $i_r^s(t) = \boldsymbol{b}_r^s(t)^{\mathrm{T}} \boldsymbol{c}_{k(t)}$. With the estimated coefficient vector $\hat{\boldsymbol{c}}_{k(t)}$, the unbiased solution of the slant ionospheric delay $i_r^s(t)$

is given by

$$\hat{i}_r^s(t) = \boldsymbol{b}_r^s(t)^{\mathrm{T}} \hat{\boldsymbol{c}}_{k(t)}. \tag{7}$$

By adapting the values of the basis functions through varying the latitude and longitude arguments, i.e., by assuming artificial IPPs covering the entire sphere, K gridded global maps of the VTEC are generated from the K sets of coefficients $\hat{\boldsymbol{c}}_\kappa$.

Alternatively, we can first determine the estimates $\hat{\tilde{i}}_r^s(t)$ of the biased ionospheric delays. These *ionospheric observables* are then used in a second step to estimate the model coefficients $\boldsymbol{c}_\kappa$ and the GF code biases $d_{r,\mathrm{GF}}^s$. This solution is mathematically identical to the direct solution above, given that $\hat{\tilde{i}}_r^s(t)$ are weighted with their inverse covariance matrix. Since all parameters in Table 1, including $\tilde{\boldsymbol{i}}_r^s$, are link-specific, they can be determined on an *arc-by-arc* basis, assuming no correlations between the observations of different links. Considering daily GIMs that are computed from a network with hundreds of receivers, for which range parameters $\tilde{\rho}_r^s(t)$ have to be set up for each link and time instance and ambiguity parameters $\tilde{a}_{r,j}^s$ for each link and frequency, this is a suitable method to avoid the solution of a large-scale system of equations.

Let the continuous arc between receiver r and satellite s contain the T observation epochs $t = 1, \ldots, T$. The variance of the observations is assumed as

$$\mathrm{D}\left[p_{r,j}^s(t)\right] = w_r^s(t)\sigma_p^2 \quad \text{and} \quad \mathrm{D}\left[\varphi_{r,j}^s(t)\right] = \epsilon w_r^s(t)\sigma_p^2, \tag{8}$$

with $w_r^s(t)$ exponential elevation dependent noise amplification factors from Euler and Goad (1991), σ_p^2 the zenith-referenced variance of the code observations, and ϵ a factor that accounts for the higher precision of the phase observations and is chosen as $\epsilon = 0.0001$. Correlations between observations are assumed absent.

Through an invertible transformation the T code observations $p_{r,j}^s(t)$ can equivalently be expressed by the time-averaged component

$$p_{r,j}^s(\bar{t}) = \bar{w}_r^s \sum_{t=1}^{T} w_r^s(t)^{-1} p_{r,j}^s(t) \tag{9}$$

with $\bar{w}_r^{s,-1} = \sum_{t=1}^{T} w_r^s(t)^{-1}$, and the $T-1$ time-differenced components

$$p_{r,j}^s(1t) = p_{r,j}^s(t) - p_{r,j}^s(1), \quad t = 2, \ldots, T, \tag{10}$$

see Khodabandeh and Teunissen (2016). The same transformation is applied to the phase observations $\varphi_{r,j}^s(t)$, the range parameters $\tilde{\rho}_r^s(t)$, and the estimable ionospheric delays $\tilde{i}_r^s(t)$.

With $\boldsymbol{p}_r^s(t) = \left[p_{r,1}^s(t), \ldots, p_{r,F}^s(t)\right]^{\mathrm{T}}$ and $\boldsymbol{\varphi}_r^s(t) = \left[p_{r,1}^s(t), \ldots, p_{r,F}^s(t)\right]^{\mathrm{T}}$, the full-rank time-averaged and time-differenced observation equations according to Table 1 are given by

$$\mathrm{E}\left[\begin{bmatrix} \boldsymbol{p}_r^s(\bar{t}) \\ \boldsymbol{\varphi}_r^s(\bar{t}) \end{bmatrix}\right] = \begin{bmatrix} \boldsymbol{e}_F \\ \boldsymbol{e}_F \end{bmatrix} \tilde{\rho}_r^s(\bar{t}) + \begin{bmatrix} \boldsymbol{\mu} \\ -\boldsymbol{\mu} \end{bmatrix} \tilde{i}_r^s(\bar{t}) + \begin{bmatrix} \boldsymbol{E} & \\ & \boldsymbol{I}_F \end{bmatrix} \begin{bmatrix} \tilde{\boldsymbol{d}}_r^s \\ \tilde{\boldsymbol{a}}_r^s \end{bmatrix} \tag{11}$$

and

$$\mathrm{E}\left[\begin{bmatrix} \boldsymbol{p}_r^s(1t) \\ \boldsymbol{\varphi}_r^s(1t) \end{bmatrix}\right] = \begin{bmatrix} \boldsymbol{e}_F \\ \boldsymbol{e}_F \end{bmatrix} \tilde{\rho}_r^s(1t) + \begin{bmatrix} \boldsymbol{\mu} \\ -\boldsymbol{\mu} \end{bmatrix} \tilde{i}_r^s(1t), \quad t = 2, \ldots, T, \tag{12}$$

with $\boldsymbol{e}_F$ an F-vector of ones, $\boldsymbol{\mu} = [\mu_1, \ldots, \mu_F]^{\mathrm{T}}$, $\tilde{\boldsymbol{d}}_r^s = [\tilde{d}_{r,3}^s, \ldots, \tilde{d}_{r,F}^s]^{\mathrm{T}}$, and $\tilde{\boldsymbol{a}}_r^s = [\tilde{a}_{r,1}^s, \ldots, \tilde{a}_{r,F}^s]^{\mathrm{T}}$. Matrix $\boldsymbol{E}$ follows from removing the first two columns of the F-dimensional identity matrix $\boldsymbol{I}_F$. The time-averaged and time-differenced observations are uncorrelated and have mutually exclusive sets of parameters, so that both systems can be solved separately.

The solution of the time-averaged ionospheric delay $\tilde{i}_r^s(\bar{t})$ and its variance are given by

$$\hat{\tilde{i}}_r^s(\bar{t}) = \frac{1}{\mu_2 - \mu_1}\left(p_{r,2}^s(\bar{t}) - p_{r,1}^s(\bar{t})\right) \tag{13}$$

$$\mathrm{D}\left[\hat{\tilde{i}}_r^s(\bar{t})\right] = \frac{2\bar{w}_r^s\sigma_p^2}{(\mu_2 - \mu_1)^2}, \tag{14}$$

while the solution of the time-differenced ionospheric delays $\tilde{i}_r^s(1t)$ and their variances and covariances are given by

$$\hat{\tilde{i}}_r^s(1t) = \frac{1}{F\gamma}\left\{2\epsilon\boldsymbol{\mu}^{\mathrm{T}}\left(\boldsymbol{p}_r^s(1t) - \boldsymbol{\varphi}_r^s(1t)\right) + (\epsilon - 1)[\boldsymbol{\mu} - \bar{\mu}\boldsymbol{e}_F]^{\mathrm{T}}\left(\epsilon\boldsymbol{p}_r^s(1t) + \boldsymbol{\varphi}_r^s(1t)\right)\right\} \tag{15}$$

$$\mathrm{D}\left[\hat{\tilde{i}}_r^s(1t)\right] = \frac{(1+\epsilon)}{F\gamma}\epsilon\sigma_p^2\left(w_r^s(1) + w_r^s(t)\right) \tag{16}$$

$$\mathrm{D}\left[\hat{\tilde{i}}_r^s(1t), \hat{\tilde{i}}_r^s(1k)\right] = \frac{(1+\epsilon)}{F\gamma}\epsilon\sigma_p^2 w_r^s(1), \quad t \neq k, \tag{17}$$

with $\gamma = (1+\epsilon)^2\sigma_\mu^2 + 4\epsilon\bar{\mu}^2$, $\bar{\mu} = \frac{1}{F}\sum_{j=1}^{F}\mu_j$, and $\sigma_\mu^2 = \frac{1}{F}\sum_{j=1}^{F}\left(\mu_j - \bar{\mu}\right)^2$. While the precision of the time-averaged component $\hat{\tilde{i}}_r^s(\bar{t})$ is driven by the code data, the time-differenced ionospheric delays $\hat{\tilde{i}}_r^s(1t)$ are on the level of the phase data. Derivations are given in the Appendix and in Khodabandeh and Teunissen (2016, 2017).

The time-averaged and time-differenced estimable ionospheric delays are expressed and parameterized as

$$\tilde{i}_r^s(\bar{t}) = i_r^s(\bar{t}) + d_{r,\mathrm{GF}}^s = \bar{w}_r^s\sum_{t=1}^{T}w_r^s(t)^{-1}\boldsymbol{b}_r^s(t)^{\mathrm{T}}\boldsymbol{c}_{k(t)} + d_{r,\mathrm{GF}}^s \tag{18}$$

$$\tilde{i}_r^s(1t) = i_r^s(1t) = \boldsymbol{b}_r^s(t)^{\mathrm{T}}\boldsymbol{c}_{k(t)} - \boldsymbol{b}_r^s(1)^{\mathrm{T}}\boldsymbol{c}_{k(1)}. \tag{19}$$

Since only the time-averaged ionospheric delay $\tilde{i}_r^s(\bar{t})$ depends on the link-specific GF code bias $d_{r,\mathrm{GF}}^s$, $\hat{\tilde{i}}_r^s(\bar{t})$ is a free variate that does not contribute to the solution of the ionospheric model coefficients $\boldsymbol{c}_\kappa$ and can simply be ignored (Teunissen, 2000), thereby also eliminating the bias parameter $d_{r,\mathrm{GF}}^s$. The model coefficients $\boldsymbol{c}_\kappa$ are therefore estimated only from the time-differenced ionospheric observables $\hat{\tilde{i}}_r^s(1t)$ describing the unbiased time-differenced ionospheric slant delays $i_r^s(1t)$, see also Khodabandeh and Teunissen (2017). The ionospheric observables $\hat{\tilde{i}}_r^s(1t)$ of different arcs are uncorrelated, so that the normal equations from all arcs are added, where within each arc the inverse covariance matrix from Eqs. 16 and 17 is used for weighting.

We now consider the model with the receiver and satellite specific code biases, cf. Table 2. The ionospheric model can again be directly estimated by replacing the biased ionospheric delay parameters $\tilde{i}_r^s(t)$ by the K sets of model coefficients $\boldsymbol{c}_\kappa$ and the GF code biases

$$\tilde{d}_{r,\mathrm{GF}} = d_{r,\mathrm{GF}} - d_{1,\mathrm{GF}}, \quad r \neq 1$$

$$\tilde{d}_{\mathrm{GF}}^s = d_{\mathrm{GF}}^s + d_{1,\mathrm{GF}}, \tag{20}$$

where the bias of the first receiver is chosen as reference to remove the inherent rank-deficiency. A different yet equivalent set of estimable biases is obtained with the commonly used zero-mean constraint on the GF satellite code biases of each constellation.

In the dual frequency case, the estimable parameters in Table 1 and Table 2 are identical, so that ionospheric observables $\hat{\tilde{i}}_r^s(t)$ can be obtained as described above. If more than two frequencies are used, the parameters $\tilde{d}_{r,j}$ and $\tilde{d}_{,j}^s$ are not link-specific, so that
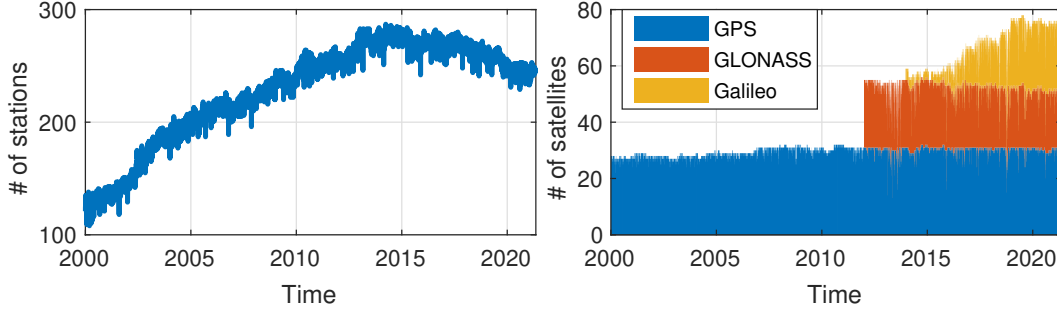
Figure 1. Numbers of stations (left) and satellites (right) used to generate the GFZ global VTEC maps.

an arc-by-arc solution is no longer possible. One can equivalently first determine the parameters of Table 1 and then jointly estimate the model coefficients $\boldsymbol{c}_\kappa$, the GF biases $\tilde{d}_{r,\mathrm{GF}}$ and $\tilde{d}^s_{\mathrm{GF}}$ (Eq. 20), and the biases $\tilde{d}_{r,j}$ and $\tilde{d}^s_{.,j}$ (Table 2) from the resulting $\hat{\tilde{i}}^s_r(t)$ and $\hat{\tilde{d}}^s_{r,j}$.

Different from Eq. 18, the estimable time-averaged ionospheric delay is now parameterized as

$$\tilde{i}^s_r(\bar{t}) = \bar{w}^s_r \sum_{t=1}^{T} w^s_r(t)^{-1} \boldsymbol{b}^s_r(t)^{\mathrm{T}} \boldsymbol{c}_{k(t)} + \tilde{d}_{r,\mathrm{GF}} + \tilde{d}^s_{\mathrm{GF}}, \qquad (21)$$

and can no longer be ignored, except for the single-receiver case. We therefore have two uncorrelated sets of observables, namely the time-averaged block with $\hat{\tilde{i}}^s_r(\bar{t})$ and possibly $\hat{\tilde{\boldsymbol{d}}}^s_r$, and the time-differenced block with $\hat{\tilde{i}}^s_r(1t)$. The solution and variance of $\hat{\tilde{\boldsymbol{d}}}^s_r$ and its covariance with $\hat{\tilde{i}}^s_r(\bar{t})$ is available through Eq. A1. The normal equations of both blocks and all arcs are added. It is shown later that the impact of the receiver-satellite bias decomposition on the ionospheric model is negligible for GIMs. It can, however, be used to obtain the GF biases or DCBs as a byproduct.

3 Operational Global VTEC Maps

The above described estimation strategy is implemented in GFZ's EPOS-P8 GNSS analysis software. Global VTEC maps with a temporal resolution of two hours, at even hours, and a spatial resolution of 2.5 degrees in latitude and 5 degrees in longitude are provided in the ionosphere map exchange format (IONEX, Schaer et al. (1998)). They are generated for the period since the beginning of 2000, and will be provided on an operational basis in the future. Daily *rapid* solutions are combined with the two neighboring solutions on the normal equation level to a *final* solution, from which mainly the first and last maps that are contained twice benefit. The settings of the processing are in line with the GFZ activities for the third IGS reprocessing campaign (Männel et al., 2020), so that GLONASS is included since 2012 and Galileo since 2014. Dual-frequency GPS L1/L2, GLONASS L1/L2, and Galileo E1/E5a data are used. The numbers of stations and satellites are shown in Figure 1. In 2021, around 250 globally distributed stations and 75 satellites are employed.

Daily receiver and satellite GF code biases/DCBs are estimated and provided for GPS to be compatible with the IGS solution. For GLONASS, the receiver-satellite decomposition of the DCBs is not valid due to the presence of inter-channel code biases caused by the FDMA scheme, so that the receiver DCBs are satellite dependent (Wang et al., 2016; X. Zhang et al., 2017). Furthermore, the impact of the receiver-satellite bias decomposition on the VTEC maps is negligible, as shown below. The biases of GLONASS
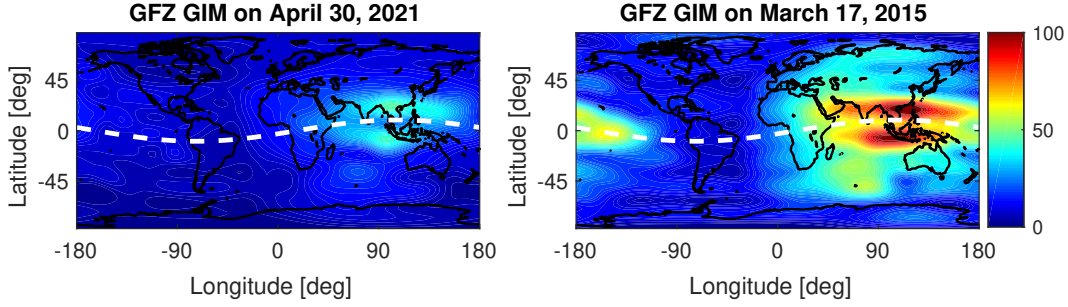
Figure 2. Two exemplary GIMs showing the VTEC in TECU for moderate ionospheric activity (left) and the St. Patrick's Day geomagnetic storm (right), both at 8:00 UTC. The dashed lines mark the geomagnetic equator.
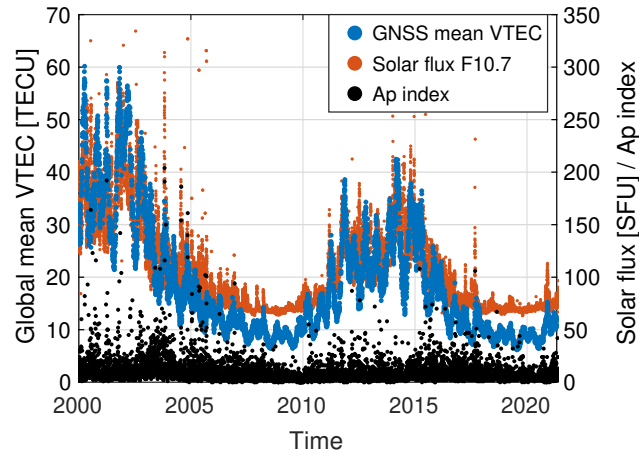

Figure 3. Time series of the GFZ GNSS-derived global mean VTEC values, of the F10.7 solar flux index in solar flux units (SFU), and of the Ap geomagnetic index.

301 and Galileo are therefore assumed arc-specific and DCBs are not estimated, cf. Section
302 2. This is conform with the definition of the future IONEX 1.1 format, in which DCBs
303 are no longer supported, but should be provided in a separate bias file. To this end, DCBs
304 between arbitrary signals of any system, in particular also for the ones that are not used
305 to generate the ionospheric solution, can be estimated after correcting the ionospheric
306 delays of $\tilde{i}_r^s$ in Table 1 and 2 with the GIMs (Keshin, 2012; Montenbruck et al., 2014),
307 and a complete set of DCBs can be generated.

308   Two exemplary GIMs, one for April 30, 2021, a day with moderate ionospheric ac-
309 tivity, and the St. Patrick's day geomagnetic storm on March 17, 2015, are shown in Fig-
310 ure 2.

311   Global mean VTEC values are obtained by a weighted mean of all grid values, where
312 the weighting coefficient is proportional to the cosine of the latitude to account for the
313 surface area represented by each grid point. Annual and seasonal variations of the GNSS
314 derived daily global mean VTEC, as well as the signature of the solar-cycle, are shown
315 in Figure 3. The values strongly resemble the characteristics of the solar radio flux, as
316 shown by the F10.7 index (Tapping, 2013). The daily equivalent planetary amplitude
317 Ap as an index of the average level of geomagnetic activity (Matzka, Stolle, et al., 2021)
318 generally shows larger values for larger mean VTEC values, and its maximum values co-
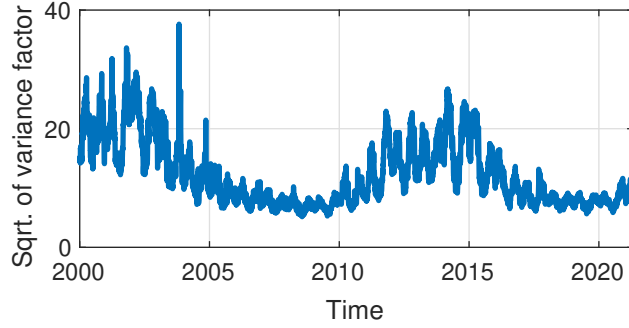319 incide with peaks of the mean VTEC and F10.7.

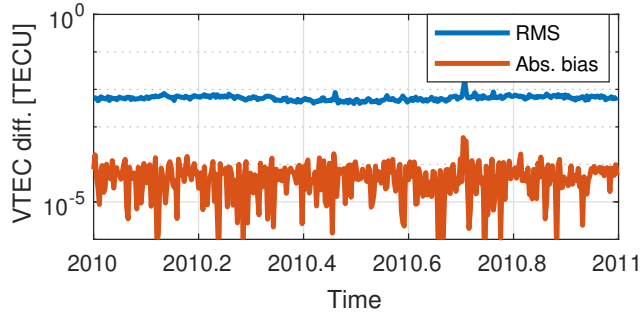**Figure 4.** Time series of the square root of the estimated variance factor of the GNSS observables.

Figure 5. Time series of daily absolute biases and RMS differences between the GFZ GIMs with daily and arc-specific code biases during the year 2010.

The single-layer spherical harmonic model representation is a strong simplification of the physical reality. The precision of the VTEC that is derived from the law of error propagation from the estimated model coefficients $\hat{c}_\kappa$ does therefore generally not represent its accuracy. For the RMS maps that are provided along with the VTEC maps, a variance factor is estimated from the residuals relative to a unit standard deviation of $\sigma_p = 1\,\mathrm{m}$ in zenith direction for the code observations and $\sqrt{\epsilon}\sigma_p = 1\,\mathrm{cm}$ for phase observations, cf. Eq. 8. With a perfect model, the estimated variance factor should be below one. In the time series in Figure 4 we see values of $5-40$ for the square root of the variance factor, meaning that the phase residuals are at the decimeter rather than the millimeter or centimeter level that would be possible from the observation precision. The close resemblance with the mean VTEC in Figure 3 shows that with increasing ionospheric activity also the modeling errors increase. The maximum corresponds to the *Halloween solar storm* at the end of October 2003 with one of the largest recorded solar flares, for which also a peak of the F10.7 and an Ap index of around 200 is observed, see Figure 3.

In order to assess the impact of assuming arc-specific code biases or the receiver-satellite bias decomposition, the year 2010 was processed with both models. The daily absolute biases between the global mean VTEC of both solutions are mostly below 10^{-4} TECU and the RMS VTEC difference is around 0.006 TECU as shown in Figure 5. Both values are clearly below the resolution of 0.1 TECU of the IONEX format, so that the benefit of the bias decomposition on the VTEC estimation through increased redundancy is negligible. This shows that essentially only the time-differenced observation data is relevant for estimating the ionospheric model, cf. Section 2.3, when applying a rigorous least-squares approach.
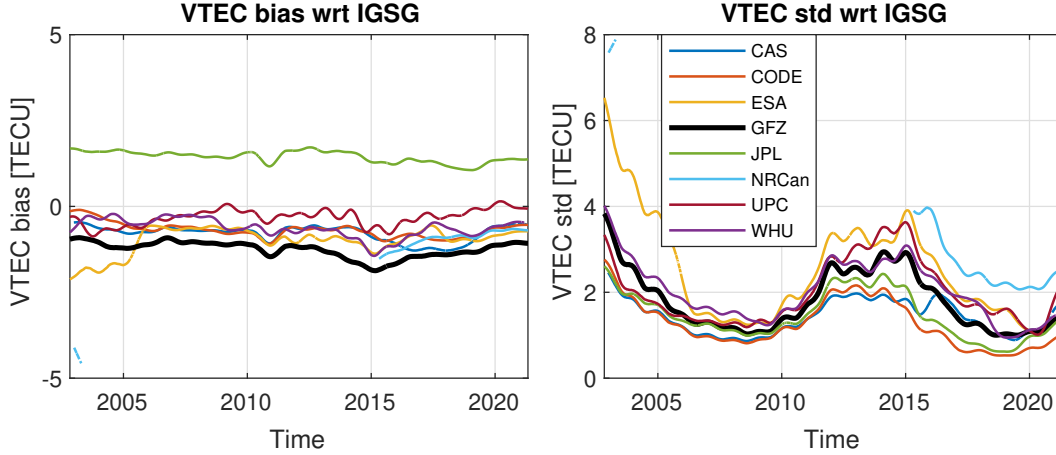
Figure 6. Smoothed time series of daily biases (left) and standard deviations (right) between the final GIMs of the seven IAACs+GFZ and the final IGS solution.

4 Comparison with the IGS GIMs

Operational GIMs are provided by several analysis centers based on different processing approaches. Within the IGS, the ionosphere working group was established in 1998. Currently, seven IGS Ionosphere Associated Analysis Centers (IAACs) provide rapid and final GIMs, which are combined to the rapid and final IGS solutions. We compare the final GFZ solution and the final GIMs of the IAACs to the final IGS solution (IGSG, Hernández-Pajares et al. (2009)). The considered solutions are:

- Chinese Academy of Sciences (CAS) with CASG (Li et al., 2015)
- Center for Orbit Determination in Europe (CODE) with CODG (Schaer et al., 1996)
- European Space Agency/European Space Operations Center (ESA/ESOC) with ESAG (Feltens, 2007)
- Jet Propulsion Laboratory (JPL) with JPLG (Mannucci et al., 1998)
- Natural Resources Canada (NRCan) with EMRG (Ghoddousi-Fard, 2014)
- Universitat Politecnica de Catalunya (UPC-IonSAT) with UPCG (Hernández-Pajares et al., 1999)
- Wuhan University (WHU) with WHUG (H. Zhang et al., 2013).

A description and comparison of the final GIMs of these seven IAACs can be found in Roma-Dollase et al. (2018).

The smoothed time series of the daily VTEC biases and standard deviations between the individual solutions and the combined solution IGSG are shown in Figure 6, starting from November 2002, which is when IGSG switched from 12 daily maps at odd hours to 13 daily maps at even hours. The biases and standard deviations are computed by means of integrating over the sphere as defined above. One has to be careful when interpreting these measures, as they merely indicate how close the solutions are to the IGS combination, but not how well they describe the reality. In addition, between end-2014 and mid-2019, the IGS combination is dominated by CODG and JPLG, so that these two solutions are by design close to the combination.

The daily VTEC biases in Figure 6 show that all eight solutions generally agree very well with the IGS solution with absolute values of less than two TECU. The bias of each solution is largely consistent over time and does not depend on the ionospheric
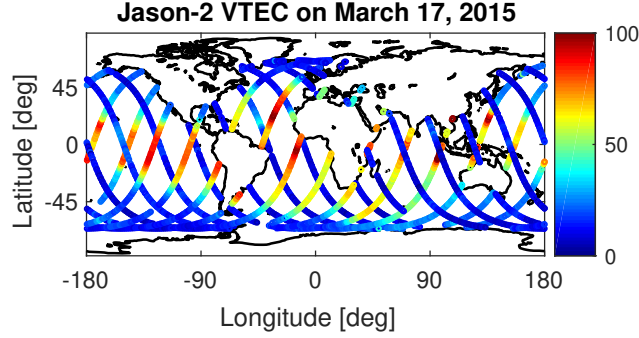
Jason-2 VTEC on March 17, 2015

Figure 7. Jason-2 VTEC in TECU during the day of the St. Patrick's day geomagnetic storm.
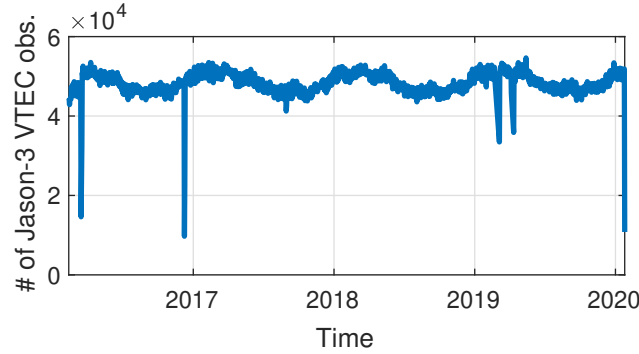

Figure 8. Daily numbers of Jason-3 VTEC observations used for validation of the GNSS GIMs.

activity. The VTEC values of JPL are about two TECU larger compared to the other solutions, whereas the VTEC values of GFZ tend to be slightly smaller than the IGS combination. The daily VTEC standard deviations confirm an agreement of the individual solutions at the few TECU level, with values of around two TECU or below during times of low ionospheric activity, cf. Figure 3, and a few TECU during high ionospheric activity. The GFZ solution is consistent with the solutions of the IAACs and the IGS combination.

5 Validation with Jason-3 Altimetry VTEC

The VTEC over the oceans can directly be observed from dual-frequency altimeters (5.3 and 13.6 GHz for the Jason satellites). Although the altimetry VTEC observations potentially suffer from instrumental biases (Azpilicueta & Brunini, 2009), and do not capture the TEC of the upper ionosphere and plasmasphere above the orbital height (1.336 km for Jason-3), they are GNSS-independent and are well suited to validate the GNSS GIMs. Exemplary Jason-2 VTEC values for all satellite passes on the day of the St. Patrick's day geomagnetic storm corresponding to Figure 2 are shown in Figure 7. We use the VTEC observations of the Jason-3 satellite that are provided by DGFI-TUM (Dettmering et al., 2011) from its launch in January 2016 until January 2021. Observations with active rain or ice flag are removed. The number of daily observations used to validate the GNSS GIMs is shown in Figure 8.

For every altimetry VTEC observation, the associated GNSS VTEC is computed through a temporal interpolation of the two closest VTEC maps, which are rotated to
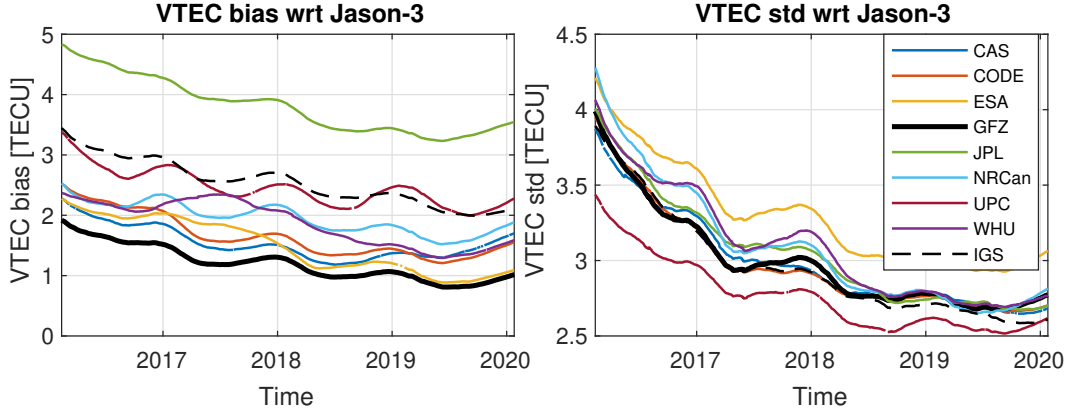
Figure 9. Smoothed time series of daily biases (left) and standard deviations (right) between the final GNSS GIMs and the Jason-3 VTEC data.
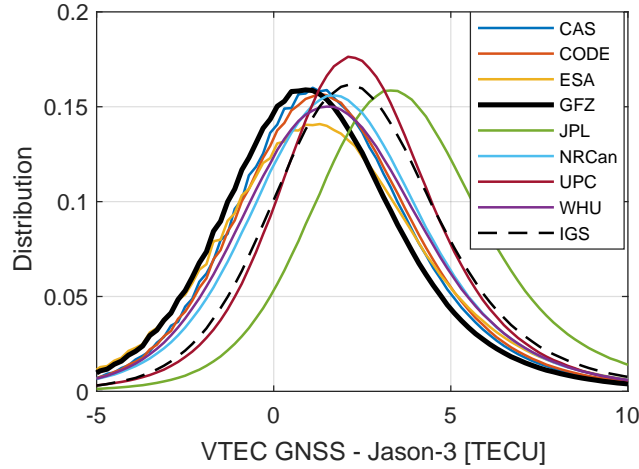

Figure 10. Distribution of the differences between the GNSS GIMs and Jason-3 VTEC data.

account for the correlation between the TEC and the Sun's position, and a spatial interpolation between the four closest grid points (Schaer et al., 1998).

Daily mean biases and standard deviations of the GNSS solutions compared to the Jason-3 VTEC are shown in Figure 9. All GNSS solutions show a positive VTEC bias, which is attributed to the situation mentioned above. The differences of the biases reflect the behavior of the VTEC biases in Figure 6. The GFZ solution has the smallest bias, whereas the bias of the JPL solution is the largest one. Due to the expected and observed bias of the Jason-3 VTEC, the more important measure to assess the quality of the GNSS GIMs is the standard deviation. The UPC solution shows the smallest values. The results of the GFZ, CAS, CODE, and IGS solutions are almost identical, and the remaining solutions have slightly larger standard deviations with the ESA solution having the largest values. Comparing Figure 9 to Figure 3 confirms that the modeling errors increase with increasing ionospheric activity. The agreement of the GNSS GIMs with the Jason-3 VTEC is at the few TECU level.

The overall distribution of all VTEC differences between the GNSS GIMs and Jason-3 is presented in Figure 10 for the nine GNSS solutions. Each curve is normalized so as to represent a valid distribution function. The associated biases, standard deviations,

Table 3. Biases, standard deviations, and RMS differences between nine GNSS GIMs and the Jason-3 VTEC observations; all values are in [TECU].

	Bias	Std	RMS
CAS	1.55	3.04	3.41
CODE	1.66	3.01	3.44
ESA	1.51	3.35	3.67
GFZ	**1.22**	**3.02**	**3.25**
JPL	3.83	3.10	4.92
NRCan	1.97	3.15	3.71
UPC	2.48	2.81	3.74
WHU	1.88	3.17	3.68
IGS	2.56	2.99	3.93

and RMS differences are given in Table 3. These results confirm the findings of Figure 9. The GFZ solution has the smallest bias. The UPC solution is most peaked, but all solutions have a standard deviation of around three TECU. In terms of the RMS values, the GFZ solution is the best, caused by the smallest bias and one of the smallest standard deviations.

6 Conclusion

In this paper, the operational GFZ GNSS GIMs were introduced and an initial assessment was provided.

A rigorous least-squares approach was formulated to estimate the coefficients of the single-layer spherical harmonic ionospheric model from uncombined multi-frequency, multi-GNSS code and phase observations. The shortcomings of the commonly used geometry-free observations combined with a phase-to-code leveling procedure were avoided with this approach. In order to avoid a large-scale adjustment problem, a two-step procedure was formulated. Biased ionospheric delays and potentially code biases for the third frequency and beyond are determined on an arc-by-arc basis, for which closed form solutions exist, and serve as an input for estimating the ionospheric model. This solution is mathematically identical to a direct solution.

If the code biases are assumed arc-specific, only the time-differenced observation data are relevant, whereas with a receiver-satellite bias decomposition also the time-averaged observation data are used. It was demonstrated, however, that the impact of this bias decomposition is negligible for the estimation of the global ionospheric model, so that the time-averaged data only become relevant if one wants to provide a set of DCB parameters along with the ionospheric solution, and can be ignored otherwise.

The GFZ GIMs were demonstrated to be consistent with the solutions of the IGS IAACs and the combined IGS solution through a comparison of daily VTEC biases and standard deviations between the individual solutions and the combined solution for a time span of more than 18 years.

An altimetry validation with around four years of Jason-3 VTEC data confirmed the quality of the GFZ GIMs, which had the smallest bias and one of the smallest standard deviations compared to the solutions of the IAACs.

The GFZ GIMs are provided at `ftp://isdcftp.gfz-potsdam.de/gnss/products/iono` (Brack et al., 2021).

Appendix A Solution of the Time-averaged System

In Eq. 11, the F ambiguity parameters $\tilde{\boldsymbol{a}}_r^s$ only appear in the F time-averaged phase observations $\boldsymbol{\varphi}_r^s(\bar{t})$. These phase observations are therefore free variates that do not contribute to the solution of the remaining parameters (Teunissen, 2000) and are omitted from the model. The resulting system with F unknowns and F equations is solved via inversion as

$$
\begin{bmatrix} \hat{\tilde{\rho}}_r^s(\bar{t}) \\ \hat{\tilde{i}}_r^s(\bar{t}) \\ \hat{\tilde{\boldsymbol{d}}}_r^s \end{bmatrix} = [\boldsymbol{e}_F,\ \boldsymbol{\mu},\ \boldsymbol{E}]^{-1}\,\boldsymbol{p}_r^s(\bar{t}) = \begin{bmatrix} \boldsymbol{\mu}_{\mathrm{IF}}^{\mathrm{T}} \\ \boldsymbol{\mu}_{\mathrm{GF}}^{\mathrm{T}} \\ \boldsymbol{E}^- \end{bmatrix}\boldsymbol{p}_r^s(\bar{t}),
\tag{A1}
$$

with $\boldsymbol{\mu}_{\mathrm{IF}} = \frac{1}{\mu_2-\mu_1}[\mu_2,-\mu_1,0,\ldots,0]^{\mathrm{T}}$, $\boldsymbol{\mu}_{\mathrm{GF}} = \frac{1}{\mu_2-\mu_1}[-1,1,0,\ldots,0]^{\mathrm{T}}$, and $\boldsymbol{E}^- = \boldsymbol{E}^{\mathrm{T}}(\boldsymbol{I}_F - \boldsymbol{e}\boldsymbol{\mu}_{\mathrm{IF}}^{\mathrm{T}} - \boldsymbol{\mu}\boldsymbol{\mu}_{\mathrm{GF}}^{\mathrm{T}})$, cf. Khodabandeh and Teunissen (2016). The variances of the estimates follow from applying the error propagation law to Eq. 8.

Appendix B Solution of the Time-differenced System

With $\boldsymbol{y}_r^s(1t) = \left[\boldsymbol{p}_r^s(1t)^{\mathrm{T}}, \boldsymbol{\varphi}_r^s(1t)^{\mathrm{T}}\right]^{\mathrm{T}}$, stacking the time-differenced observations for $t = 2,\ldots,T$ in Eq. 12 yields

$$
\mathrm{E}\Bigg[\underbrace{\begin{bmatrix} \boldsymbol{y}_r^s(12) \\ \vdots \\ \boldsymbol{y}_r^s(1T) \end{bmatrix}}_{\boldsymbol{y}_{r,\mathrm{td}}^s}\Bigg] = \underbrace{\left[\boldsymbol{I}_{T-1} \otimes \begin{bmatrix} \boldsymbol{e}_F \\ \boldsymbol{e}_F \end{bmatrix}\right]}_{\boldsymbol{A}}\begin{bmatrix} \tilde{\rho}_r^s(12) \\ \vdots \\ \tilde{\rho}_r^s(1T) \end{bmatrix} + \underbrace{\left[\boldsymbol{I}_{T-1} \otimes \begin{bmatrix} \boldsymbol{\mu} \\ -\boldsymbol{\mu} \end{bmatrix}\right]}_{\boldsymbol{B}}\underbrace{\begin{bmatrix} \tilde{i}_r^s(12) \\ \vdots \\ \tilde{i}_r^s(1T) \end{bmatrix}}_{\tilde{\boldsymbol{i}}_{r,\mathrm{td}}^s}.
\tag{B1}
$$

The covariance matrix of $\boldsymbol{y}_{r,\mathrm{td}}^s$ follows from Eq. 8 as

$$
\boldsymbol{Q}_{r,\mathrm{td}}^s = \sigma_p^2 \boldsymbol{D}^{\mathrm{T}}\boldsymbol{W}_r^s\boldsymbol{D} \otimes \begin{bmatrix} \boldsymbol{I}_F & \\ & \epsilon\boldsymbol{I}_F \end{bmatrix},
\tag{B2}
$$

with the differencing operator $\boldsymbol{D}^{\mathrm{T}} = [-\boldsymbol{e}_{T-1}, \boldsymbol{I}_{T-1}]$ and $\boldsymbol{W}_r^s$ a T-dimensional square matrix with the T values of $w_r^s(t)$ on its diagonal. We further have

$$
\boldsymbol{A}^{\mathrm{T}}\boldsymbol{Q}_{r,\mathrm{td}}^{s,-1}\boldsymbol{A} = (\boldsymbol{D}^{\mathrm{T}}\boldsymbol{W}_r^s\boldsymbol{D})^{-1}\tfrac{\epsilon+1}{\epsilon\sigma_p^2}F
$$

$$
\boldsymbol{A}^{\mathrm{T}}\boldsymbol{Q}_{r,\mathrm{td}}^{s,-1}\boldsymbol{B} = (\boldsymbol{D}^{\mathrm{T}}\boldsymbol{W}_r^s\boldsymbol{D})^{-1}\tfrac{\epsilon-1}{\epsilon\sigma_p^2}F\bar{\mu}
$$

$$
\boldsymbol{B}^{\mathrm{T}}\boldsymbol{Q}_{r,\mathrm{td}}^{s,-1}\boldsymbol{B} = (\boldsymbol{D}^{\mathrm{T}}\boldsymbol{W}_r^s\boldsymbol{D})^{-1}\tfrac{\epsilon+1}{\epsilon\sigma_p^2}F(\bar{\mu}^2 + \sigma_\mu^2),
\tag{B3}
$$

where the last equality follows from $\boldsymbol{\mu}^{\mathrm{T}}\boldsymbol{\mu} = F(\bar{\mu}^2 + \sigma_\mu^2)$.

The least-squares solutions $\hat{\tilde{i}}_r^s(1t)$ in Eq. 15 are the rows of

$$
\hat{\tilde{\boldsymbol{i}}}_{r,\mathrm{td}}^s = \left(\bar{\boldsymbol{B}}^{\mathrm{T}}\boldsymbol{Q}_{r,\mathrm{td}}^{s,-1}\bar{\boldsymbol{B}}\right)^{-1}\bar{\boldsymbol{B}}^{\mathrm{T}}\boldsymbol{Q}_{r,\mathrm{td}}^{s,-1}\boldsymbol{y}_{r,\mathrm{td}}^s,
\tag{B4}
$$

where $\bar{\boldsymbol{B}} = \boldsymbol{B} - \boldsymbol{A}(\boldsymbol{A}^{\mathrm{T}}\boldsymbol{Q}_{r,\mathrm{td}}^{s,-1}\boldsymbol{A})^{-1}\boldsymbol{A}^{\mathrm{T}}\boldsymbol{Q}_{r,\mathrm{td}}^{s,-1}\boldsymbol{B}$ follows from Eq. B3 as $\bar{\boldsymbol{B}} = \boldsymbol{B} - \boldsymbol{A}\tfrac{\epsilon-1}{\epsilon+1}\bar{\mu}$. Using this expression and Eq. B3, the inverse covariance matrix of $\hat{\tilde{i}}_r^s(1t)$ is derived as

$$
\bar{\boldsymbol{B}}^{\mathrm{T}}\boldsymbol{Q}_{r,\mathrm{td}}^{s,-1}\bar{\boldsymbol{B}} = (\boldsymbol{D}^{\mathrm{T}}\boldsymbol{W}_r^s\boldsymbol{D})^{-1}\frac{F\big(\overbrace{(1+\epsilon)^2\sigma_\mu^2 + 4\epsilon\bar{\mu}^2}^{\gamma}\big)}{\epsilon\sigma_p^2(1+\epsilon)},
\tag{B5}
$$

cf. Eqs. 16 and 17. Similar to Eq. B3 we have

$$
\boldsymbol{A}^{\mathrm{T}}\boldsymbol{Q}_{r,\mathrm{td}}^{s,-1} = \sigma_p^{-2}(\boldsymbol{D}^{\mathrm{T}}\boldsymbol{W}_r^s\boldsymbol{D})^{-1} \otimes \left[\boldsymbol{e}_F^{\mathrm{T}}, \tfrac{1}{\epsilon}\boldsymbol{e}_F^{\mathrm{T}}\right]
$$

$$
\boldsymbol{B}^{\mathrm{T}}\boldsymbol{Q}_{r,\mathrm{td}}^{s,-1} = \sigma_p^{-2}(\boldsymbol{D}^{\mathrm{T}}\boldsymbol{W}_r^s\boldsymbol{D})^{-1} \otimes \left[\boldsymbol{\mu}^{\mathrm{T}}, -\tfrac{1}{\epsilon}\boldsymbol{\mu}^{\mathrm{T}}\right].
\tag{B6}
$$

Using Eqs. B5 and B6, the $(t-1)$th row of Eq. B4 reads

$$\hat{\tilde{i}}_r^s(1t) = \frac{\epsilon(1+\epsilon)}{F\gamma}\Big\{\big(\boldsymbol{\mu}^{\mathrm{T}} - \tfrac{\epsilon-1}{\epsilon+1}\bar{\mu}\boldsymbol{e}_F^{\mathrm{T}}\big)\boldsymbol{p}_r^s(1t) + \tfrac{1}{\epsilon}\big(-\boldsymbol{\mu}^{\mathrm{T}} - \tfrac{\epsilon-1}{\epsilon+1}\bar{\mu}\boldsymbol{e}_F^{\mathrm{T}}\big)\boldsymbol{\varphi}_r^s(1t)\Big\}, \qquad \text{(B7)}$$

from which Eq. 15 is obtained by rearranging the terms.

References

Azpilicueta, F., & Brunini, C. (2009). Analysis of the bias between TOPEX and GPS vTEC determinations. *J Geod*, *83*(2), 121–127. doi: 10.1007/s00190-008-0244-7

Azpilicueta, F., Brunini, C., & Radicella, S. M. (2006). Global ionospheric maps from GPS observations using modip latitude. *Adv Space Res*, *38*(11), 2324–2331. doi: 10.1016/j.asr.2005.07.069

Baarda, W. (1973). S-transformations and criterion matrices. *Netherlands Geodetic Commission, Publications on Geodesy, New Series*, *5*(1).

Brack, A., Männel, B., Bradke, M., Brandt, A., & Nischan, T. (2021). GFZ global ionosphere maps. *GFZ Data Services*. doi: in.preparation

Bradke, M. (2020). SEMISYS - Sensor Meta Information System. *GFZ Data Services*. doi: 10.5880/GFZ.1.1.2020.005

Brunini, C., & Azpilicueta, F. (2010). GPS slant total electron content accuracy using the single layer model under different geomagnetic regions and ionospheric conditions. *J Geod*, *84*(5), 293–304. doi: 10.1007/s00190-010-0367-5

Brunini, C., & Azpilicueta, F. J. (2009). Accuracy assessment of the GPS-based slant total electron content. *J Geod*, *83*(8), 773–785. doi: 10.1007/s00190-008-0296-8

Ciraolo, L., Azpilicueta, F., Brunini, C., Meza, A., & Radicella, S. M. (2007). Calibration errors on experimental slant total electron content (TEC) determined with GPS. *J Geod*, *81*(2), 111–120. doi: 10.1007/s00190-006-0093-1

Davies, K., & Hartmann, G. K. (1997). Studying the ionosphere with the Global Positioning System. *Radio Sci*, *32*(4), 1695–1703. doi: 10.1029/97RS00451

Dettmering, D., Schmidt, M., Heinkelmann, R., & Seitz, M. (2011). Combination of different space-geodetic observations for regional ionosphere modeling. *J Geod*, *85*(12), 989–998. doi: 10.1007/s00190-010-0423-1

Euler, H. J., & Goad, C. C. (1991). On optimal filtering of GPS dual frequency observations without using orbit information. *B Geod*, *65*(2), 130–143. doi: 10.1007/BF00806368

Feltens, J. (2007). Development of a new three-dimensional mathematical ionosphere model at European Space Agency/European Space Operations Centre. *Space Weather*, *5*(12). doi: 10.1029/2006SW000294

Ghoddousi-Fard, R. (2014). GPS ionospheric mapping at Natural Resources Canada. In *Proc. of IGS Workshop 2014*. Pasadena, CA, USA.

Goss, A., Schmidt, M., Erdogan, E., Görres, B., & Seitz, F. (2019). High-resolution vertical total electron content maps based on multi-scale B-spline representations. *Ann Geophys*, *37*(4), 699–717. doi: 10.5194/angeo-37-699-2019

Hauschild, A. (2017). Basic Observation Equations. In *Springer handbook of global navigation satellite systems* (pp. 561–582). Springer.

Hernández-Pajares, M., Juan, J., & Sanz, J. (1999). New approaches in global ionospheric determination using ground GPS data. *J Atmos Sol-Terr Phy*, *61*(16), 1237–1247. doi: 10.1016/S1364-6826(99)00054-1

Hernández-Pajares, M., Juan, J. M., Sanz, J., Aragón-Àngel, À., García-Rigo, A., Salazar, D., & Escudero, M. (2011). The ionosphere: effects, GPS modeling and the benefits for space geodetic techniques. *J Geod*, *85*(12), 887–907. doi: 10.1007/s00190-011-0508-5

Hernández-Pajares, M., Juan, J. M., Sanz, J., Orus, R., Garcia-Rigo, A., Feltens, J., ... Krankowski, A. (2009). The IGS VTEC maps: a reliable source of ionospheric information since 1998. *J Geod*, *83*(3-4), 263–275. doi: 10.1007/s00190-008-0266-1

Jakowski, N., Schlüter, S., & Sardon, E. (1999). Total electron content of the ionosphere during the geomagnetic storm on 10 January 1997. *J Atmos Sol-Terr Phy*, *61*(3-4), 299–307. doi: 10.1016/S1364-6826(98)00130-8

Johnston, G., Riddell, A., & Hausler, G. (2017). The international GNSS service. In *Springer handbook of global navigation satellite systems* (pp. 967–982). Springer.

Keshin, M. (2012). A new algorithm for single receiver DCB estimation using IGS TEC maps. *GPS Solut*, *16*(3), 283–292. doi: 10.1007/s10291-011-0230-z

Khodabandeh, A., & Teunissen, P. J. G. (2015). An analytical study of PPP-RTK corrections: precision, correlation and user-impact. *J Geod*, *89*(11), 1109–1132. doi: 10.1007/s00190-015-0838-9

Khodabandeh, A., & Teunissen, P. J. G. (2016). Array-Aided Multifrequency GNSS Ionospheric Sensing: Estimability and Precision Analysis. *IEEE Trans Geosci and Remote Sens*, *54*(10), 5895–5913. doi: 10.1109/TGRS.2016.2574809

Khodabandeh, A., & Teunissen, P. J. G. (2017). S-system theory applied to array-based GNSS ionospheric sensing. *Stud Geophys Geod*, *61*(3), 429–452. doi: 10.1007/s11200-016-1176-y

Komjathy, A. (1997). *Global ionospheric total electron content mapping using the Global Positioning System* (Dissertation, Dep. of Geodesy and Geomatics Engineering Technical Report No. 188). University of New Brunswick.

Lanyi, G. E., & Roth, T. (1988). A comparison of mapped and measured total ionospheric electron content using global positioning system and beacon satellite observations. *Radio Sci*, *23*(4), 483–492. doi: 10.1029/RS023i004p00483

Laundal, K. M., & Richmond, A. D. (2017). Magnetic Coordinate Systems. *Space Sci Rev*, *206*, 27–59. doi: 10.1007/s11214-016-0275-y

Li, Z., Yuan, Y., Wang, N., Hernandez-Pajares, M., & Huo, X. (2015). SHPTS: towards a new method for generating precise global ionospheric TEC map based on spherical harmonic and generalized trigonometric series functions. *J Geod*, *89*(4), 331–345. doi: 10.1007/s00190-014-0778-9

Männel, B., Brandt, A., Bradke, M., Sakic, P., Brack, A., & Nischan, T. (2020). Status of IGS Reprocessing Activities at GFZ. In *Iag symposia*. doi: 10.1007/1345{_}2020{_}98

Männel, B., Brandt, A., Bradke, M., Sakic, P., Brack, A., & Nischan, T. (2021). GFZ repro3 product series for the International GNSS Service (IGS). *GFZ Data Services*. doi: 10.5880/GFZ.1.1.2021.001

Mannucci, A. J., Wilson, B. D., Yuan, D. N., Ho, C. H., Lindqwister, U. J., & Runge, T. F. (1998). A global mapping technique for GPS-derived ionospheric total electron content measurements. *Radio Sci*, *33*(3), 565–582. doi: 10.1029/97RS02707

Matzka, J., Bronkalla, O., Tornow, K., Elger, K., & Stolle, C. (2021). Geomagnetic Kp index. *GFZ Data Services*. doi: 10.5880/Kp.0001

Matzka, J., Stolle, C., Yamazaki, Y., Bronkalla, O., & Morschhauser, A. (2021). The

Geomagnetic Kp Index and Derived Indices of Geomagnetic Activity. *Space Weather*, *19*(5), e2020SW002641. doi: 10.1029/2020SW002641

Montenbruck, O., & Hauschild, A. (2013). Code Biases in Multi-GNSS Point Positioning. In *Proc. of ION-ITM 2013* (pp. 616–628).

Montenbruck, O., Hauschild, A., & Steigenberger, P. (2014). Differential Code Bias Estimation using Multi-GNSS Observations and Global Ionosphere Maps. *Navigation*, *61*(3), 191–201. doi: 10.1002/navi.64

Roma-Dollase, D., Hernández-Pajares, M., Krankowski, A., Kotulak, K., Ghoddousi-Fard, R., Yuan, Y., ... Gomez-Cama, J. M. (2018). Consistency of seven different GNSS global ionospheric mapping techniques during one solar cycle. *J Geod*, *92*(6), 691–706. doi: 10.1007/s00190-017-1088-9

Sardon, E., Rius, A., & Zarraoa, N. (1994). Estimation of the transmitter and receiver differential biases and the ionospheric total electron content from Global Positioning System observations. *Radio Sci*, *29*(03), 577–586. doi: 10.1029/94RS00449

Schaer, S. (1999). *Mapping and Predicting the Earth's Ionosphere Using the Global Positioning System* (Dissertation). Astronomical Inst. Univ. Bern.

Schaer, S., Beutler, G., Rothacher, M., & Springer, T. A. (1996). Daily global ionosphere maps based on GPS carrier phase data routinely produced by the CODE Analysis Center. In *Proc. of IGS AC Workshop 1996.* Silver Spring, MD, USA.

Schaer, S., Gurtner, W., & Feltens, J. (1998). IONEX: The ionosphere map exchange format version 1. In *Proc. of IGS AC Workshop 1998.* Darmstadt, Germany.

Tapping, K. F. (2013). The 10.7 cm solar radio flux (F10.7). *Space Weather*, *11*(7), 394–406. doi: 10.1002/swe.20064

Teunissen, P. J. G. (1985). Generalized inverses, adjustment, the datum problem and S-transformations. In *Optimization and design of geodetic networks* (pp. 11–55). Springer.

Teunissen, P. J. G. (2000). *Adjustment theory, an introduction.* Delft Academic Press, Series on Mathematical Geodesy and Positioning.

Wang, N., Yuan, Y., Li, Z., Montenbruck, O., & Tan, B. (2016). Determination of differential code biases with multi-GNSS observations. *J Geod*, *90*(3), 209–228. doi: 10.1007/s00190-015-0867-4

Wickert, J., Dick, G., Schmidt, T., Asgarimehr, M., Antonoglou, N., Arras, C., ... Zus, F. (2020). GNSS Remote Sensing at GFZ: Overview and Recent Results. *zfv - Zeitschrift für Geodäsie, Geoinformation und Landmanagement*, *145*(5), 266–278. doi: 10.12902/zfv-0320-2020

Zhang, H., Xu, P., Han, W., Ge, M., & Shi, C. (2013). Eliminating negative VTEC in global ionosphere maps using inequality-constrained least squares. *Adv Space Res*, *51*(6), 988–1000. doi: 10.1016/j.asr.2012.06.026

Zhang, X., Xie, W., Ren, X., Li, X., Zhang, K., & Jiang, W. (2017). Influence of the GLONASS inter-frequency bias on differential code bias estimation and ionospheric modeling. *GPS Solut*, *21*(3), 1355–1367. doi: 10.1007/s10291-017-0618-5